

# Observation of ultrafast interfacial Meitner-Auger energy transfer in a van der Waals heterostructure

Shuo Dong<sup>1\*</sup>, Samuel Beaulieu<sup>1,2</sup>, Malte Selig<sup>3</sup>, Philipp Rosenzweig<sup>4</sup>, Dominik Christiansen<sup>3</sup>, Tommaso Pincelli<sup>1</sup>, Maciej Dendzik<sup>1,5</sup>, Jonas D. Ziegler<sup>6</sup>, Julian Maklar<sup>1</sup>, R. Patrick Xian<sup>1,7</sup>, Alexander Neef<sup>1</sup>, Avaise Mohammed<sup>4</sup>, Armin Schulz<sup>4</sup>, Mona Stadler<sup>8</sup>, Michael Jetter<sup>8</sup>, Peter Michler<sup>8</sup>, Takashi Taniguchi<sup>9</sup>, Kenji Watanabe<sup>10</sup>, Hidenori Takagi<sup>4,11,12</sup>, Ulrich Starke<sup>4</sup>, Alexey Chernikov<sup>6,13</sup>, Martin Wolf<sup>1</sup>, Hiro Nakamura<sup>4,14</sup>, Andreas Knorr<sup>3</sup>, Laurenz Rettig<sup>1\*</sup> & Ralph Ernstorfer<sup>1,15\*</sup>

<sup>1</sup>*Fritz-Haber-Institut der Max-Planck-Gesellschaft, Faradayweg 4-6, 14195 Berlin, Germany*

<sup>2</sup>*Université de Bordeaux - CNRS - CEA, CELIA, UMR5107, F33405, Talence, France*

<sup>3</sup>*Nichtlineare Optik und Quantenelektronik, Institut für Theoretische Physik, Technische Universität Berlin, 10623 Berlin, Germany*

<sup>4</sup>*Max Planck Institute for Solid State Research, 70569 Stuttgart, Germany*

<sup>5</sup>*Department of Applied Physics, KTH Royal Institute of Technology, Hannes Alfvéns väg 12, 114 19 Stockholm, Sweden*

<sup>6</sup>*Department of Physics, University of Regensburg, Regensburg D-93053, Germany*

<sup>7</sup>*Department of Engineering, University of Cambridge, Trumpington Street, Cambridge CB2 1PZ, United Kingdom*

<sup>8</sup>*Institute of Semiconductor Optics and Functional Interfaces, Research Center SCoPE and IQST, University of Stuttgart, 70569 Stuttgart, Germany*

<sup>9</sup>*International Center for Materials Nanoarchitectonics, National Institute for Materials Science,*

*1-1 Namiki, Tsukuba 305-0044, Japan*

<sup>10</sup>*Research Center for Functional Materials, National Institute for Materials Science, 1-1 Namiki, Tsukuba 305-0044, Japan*

<sup>11</sup>*Department of Physics, University of Tokyo, 113-0033 Tokyo, Japan*

<sup>12</sup>*Institute for Functional Matter and Quantum Technologies, University of Stuttgart, 70569 Stuttgart, Germany*

<sup>13</sup>*Institute for Applied Physics, Dresden University of Technology, Dresden, 01187, Germany*

<sup>14</sup>*Department of Physics, University of Arkansas, Fayetteville, Arkansas 72701, USA*

<sup>15</sup>*Institut für Optik und Atomare Physik, Technische Universität Berlin, 10623 Berlin, Germany*

*\*To whom correspondence should be addressed;*

*E-mail: dong@fhi-berlin.mpg.de, rettig@fhi-berlin.mpg.de, ernstorfer@fhi-berlin.mpg.de.*

Atomically thin layered van der Waals heterostructures feature exotic and emergent optoelectronic properties. With growing interest in these novel quantum materials, the microscopic understanding of fundamental interfacial coupling mechanisms is of capital importance. Here, using multidimensional photoemission spectroscopy, we provide a layer- and momentum-resolved view on ultrafast interlayer electron and energy transfer in a monolayer-WSe<sub>2</sub>/graphene heterostructure. Depending on the nature of the optically prepared state, we find the different dominating transfer mechanisms: while electron injection from graphene to WSe<sub>2</sub> is observed after photoexcitation of quasi-free hot carriers in the graphene layer, we establish an interfacial Meitner-Auger energy transfer process following the excitation of excitons in WSe<sub>2</sub>. By analysing the time-energy-momentum distributions of excited-state carriers with a rate-equation model, we distinguish these two types of interfacial dynamics and identify the ultrafast conversion of excitons in WSe<sub>2</sub> to valence band transitions in graphene. Microscopic calculations find interfacial dipole-monopole coupling underlying the Meitner-Auger energy transfer to dominate over conventional Förster- and Dexter-type interactions, in agreement with the experimental observations. The energy transfer mechanism revealed here might enable new hot-carrier-based device concepts with van der Waals heterostructures.

The unique physical properties of atomically thin two-dimensional (2D) materials<sup>1,2</sup> and constantly improving fabrication methods<sup>3,4</sup> have led to a great interest in novel quantum materials based on van der Waals (vdW) heterostructures<sup>5</sup>. By stacking 2D materials, vdW heterostructures inherit the properties from individual constituents, and exotic physical phenomena may emerge

due to the interfacial interaction<sup>5-7</sup>. An emblematic example is the emergence of superconductivity in twisted bilayer graphene when stacked at the so-called ‘magic angle’<sup>8</sup>. As another example, interlayer excitons, which are spatially separated yet Coulomb-bound electron-hole pairs in semiconducting transition metal dichalcogenide (TMDC) heterostructures allow exceptional control of optoelectronic properties<sup>9-11</sup>. Out of the vdW heterostructure library, a basic optoelectronic building block is a monolayer (ML) semiconducting TMDC in contact with graphene<sup>12</sup>. This hybrid structure represents a model system as it combines the strong light-matter coupling of TMDCs and the high mobility of massless Dirac carriers of graphene<sup>13</sup>. The gapless electronic structure of graphene allows for harvesting low-energy photons, extending the spectral range covered by conventional photodetectors to the near-infrared wavelength, which is highly beneficial for photovoltaic applications<sup>14</sup>.

Optoelectronic functionality in vdW heterostructures arises from careful design and control of optical transitions and interfacial transfer processes. Particularly, interfacial charge (ICT) and energy transfer (IET) are key processes which have triggered extensive experimental and theoretical efforts<sup>15-20</sup>. Using time-resolved optical spectroscopies, a strong reduction of the exciton lifetime<sup>21</sup> and optically active charge-transfer excitations of TMDC/graphene heterostructures have been observed<sup>22,23</sup>, suggesting strong interlayer coupling and the underlying mechanisms have been discussed<sup>24-26</sup>. Moreover, the efficiency of IET processes like Förster-type coupling (based on electronic dipole-dipole interaction) has recently been investigated theoretically, pointing out the importance of energy-momentum conservation between participating quasiparticles<sup>15</sup>. Therefore, a momentum resolved probe is required to directly monitor the dynamics and reveal

the mechanism of interfacial transfer process in vdW heterostructures, including those involving momentum-forbidden dark states.

Here, we use time- and angle-resolved photoemission spectroscopy (trARPES) to investigate ultrafast interlayer carrier interactions in an epitaxially grown ML-WSe<sub>2</sub>/graphene heterostructure. Our trARPES setup combines a high-repetition-rate (500 kHz) femtosecond extreme ultraviolet (XUV) source<sup>27</sup> coupled to a time-of-flight momentum microscope<sup>28</sup> (see Methods). It allows the measurement of the four-dimensional (4D) photoemission intensity  $I(E_{kin}, k_x, k_y, \Delta t)$ , where  $E_{kin}$  is the outgoing photoelectron kinetic energy,  $k_x, k_y$  are the in-plane momenta and  $\Delta t$  is the pump-probe delay, as shown in Fig.1**a,b**. The probe photon energy of 21.7 eV allows accessing the entire Brillouin zone of the heterostructure and the variable pump wavelength allows us to photoexcite the heterostructure in a state-resolved manner. In the following, we present a time-, energy-, and momentum-resolved study on the excited-state dynamics in the heterostructure with two different pump photon energies: below the optical bandgap of WSe<sub>2</sub> (1.2 eV) and in resonance with its first excitonic transition (1.55 eV).

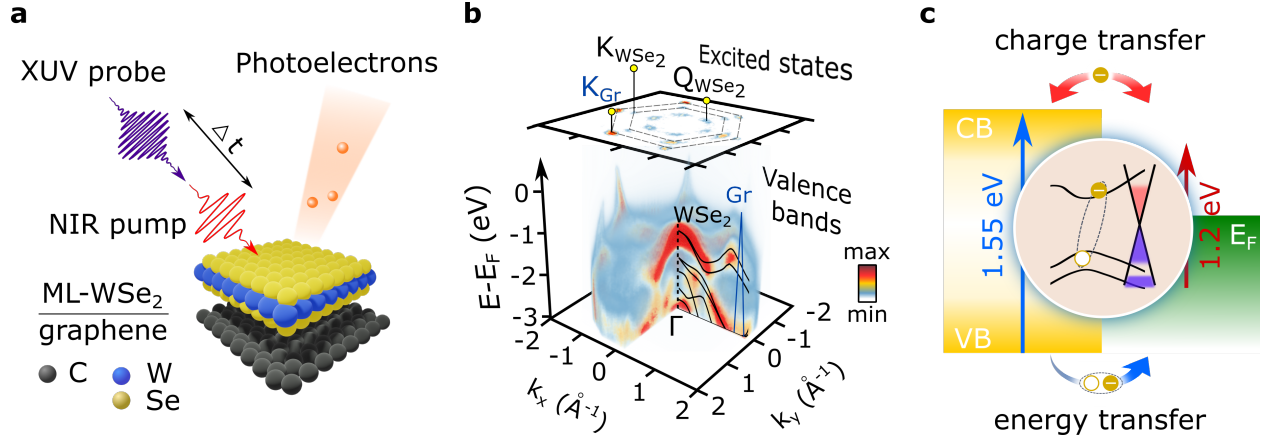


**Fig. 1: Time- and angle-resolved photoemission measurement of interlayer charge and energy transfer in a ML-WSe<sub>2</sub>/graphene heterostructure.** **a**, Following the near-infrared pump, electrons are photoionized by the delayed XUV probe pulses and collected by a three-dimensional (3D) ( $E_{kin}, k_x, k_y$ ) detector as a function of pump-probe delay  $\Delta t$ . **b**, The 3D snapshot of the 4D data,  $I(E_{kin}, k_x, k_y, \Delta t = 0 \text{ fs})$  presents the valence band structures from the  $\Gamma$  point to the Brillouin zone boundary of WSe<sub>2</sub>, as well as the linearly dispersing graphene bands. The excited state population can be clearly mapped at the  $K_{WSe_2}$  and  $Q_{WSe_2}$  valleys, and the  $\pi^*$  band of graphene ( $K_{Gr}$ ). **c**, By changing the pump wavelength, we can selectively prepare different initial excited states: quasi-free carriers in graphene with below-bandgap excitation (red arrow) or excitons in WSe<sub>2</sub> using excitation on the excitonic resonance (blue arrow).

### Interlayer quasi-free carrier transfer

First, we photoexcite the heterostructure with the pump photon energy centred at  $\hbar\omega_{pump}=1.2 \text{ eV}$  (pump pulse duration 200 fs FWHM), well below the optical bandgap of WSe<sub>2</sub><sup>29</sup>. The NIR-

pump/XUV-probe experiments were performed with a pump fluence of  $F = 5.3 \text{ mJ/cm}^2$  and at room temperature. Fig.2a-d show energy-resolved photoemission signals along the  $K' - K$  cut of the Brillouin zone, at selected time delays. The momentum distributions above  $E_F$  within the first 400 fs reveal that the excited states are localized in three different types of valleys: the Dirac cones of graphene at its K points ( $K_{Gr}$ ) and the K and Q valleys of WSe<sub>2</sub> ( $K_{WSe_2}$ ,  $Q_{WSe_2}$ ), as shown in Fig.2e. The  $Q_{WSe_2}$  valley localizes between the  $K_{WSe_2}$  valley and the  $\Gamma$  point. By performing energy-momentum integration in selected regions of interest (ROIs), we extracted excited-state dynamics within these three valleys (Fig.2f). Upon arrival of the pump pulses, the excited-state population rapidly builds up at  $K_{Gr}$  (black curve) and decays with a time scale of  $\sim 200$  fs. Strikingly, the conduction band minima (CBMs) at  $K_{WSe_2}$  (red curve) and  $Q_{WSe_2}$  valleys (green curve) are also being populated, however, with a delay of  $\Delta t = 51 \pm 9$  fs (see SI) compared to the rise of hot-carrier population in graphene. Since below-bandgap pump photon energy does not allow the direct photoexcitation of WSe<sub>2</sub>, the delayed electron populations in the conduction bands arise through charge transfer from graphene to WSe<sub>2</sub>. Two/multiple photon excitation can safely be ruled out (details see SI). The excited-state population of the  $Q_{WSe_2}$  valleys (Fig.2f) could be raised via ICT from the graphene layer and the intervalley scattering from the  $K_{WSe_2}$  valleys<sup>30,31</sup>.

These observations support the following picture of the underlying processes with a below-bandgap excitation: light is absorbed by graphene and populates unoccupied states at  $E_{Gr}^{el} = E_D + \hbar\omega_{pump}/2$ , leaving holes at  $E_{Gr}^h = E_D - \hbar\omega_{pump}/2$  (Dirac energy  $E_D > 0$  for a p-doped system or  $E_D < 0$  for an n-doped system). The energy position of the Dirac point in our heterostructure is estimated to be  $\sim -0.1$  eV below the Fermi level, obtained from the conical crossing<sup>32,33</sup>

(see SI). The photoexcited carriers quickly reach a quasi-thermalized states in  $\sim 10$  fs<sup>34</sup> and could further increase their energy via intraband electron-electron scattering and interband Auger recombination in few tens of femtoseconds<sup>35,36</sup>. Once electrons gained a sufficient amount of energy to overcome the energy barrier, they scatter to WSe<sub>2</sub> via a phonon-assisted tunneling process, filling the single-particle CBMs at  $K_{\text{WSe}_2}$  and  $Q_{\text{WSe}_2}$ . This ICT mechanism is called *interlayer hot carrier injection*, and is schematically illustrated in Fig.2g. The excited electrons in WSe<sub>2</sub> may subsequently scatter back to graphene and relax down towards the Fermi energy ( $E_F$ ). Based on the observed carrier dynamics, we performed microscopic calculations of the phonon-assisted interlayer tunneling process, allowing us to estimate the electronic wavefunction overlap between the involved conduction bands of WSe<sub>2</sub> and graphene to be around 4% (see SI for details).



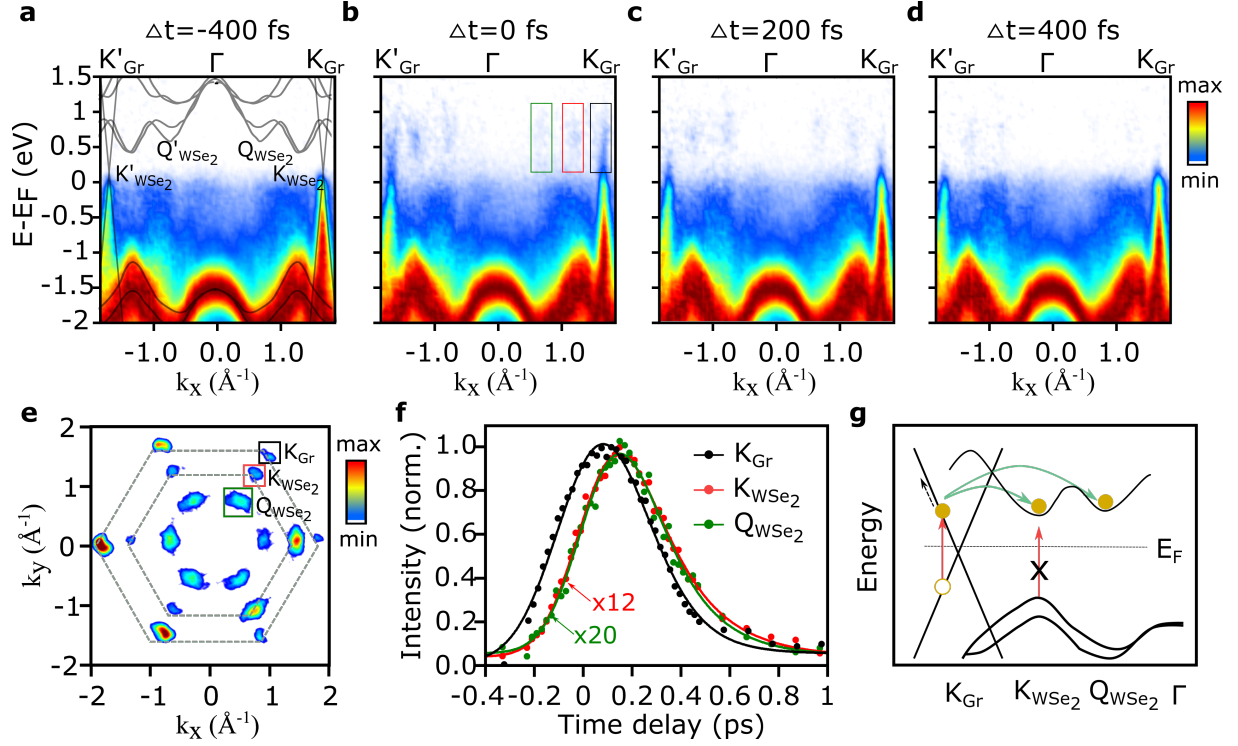


**Fig. 2: Layer- and valley-resolved ultrafast dynamics upon below-bandgap pumping.** **a-d**, Energy-momentum cuts of the photoemission signal along the  $K'_{Gr}$ - $K'_{WSe_2}$ - $\Gamma$ - $K_{WSe_2}$ - $K_{Gr}$  high symmetry direction, at selected pump-probe time delays. **a**, The 2D spectrum at negative time delay reveals the equilibrium band structure of ML-WSe<sub>2</sub> as well as the linearly dispersing  $\pi$  band of graphene. The grey lines represent the DFT-calculated band structures (details in methods). Snapshots of the energy-momentum cuts at time delays of **b**  $\Delta t = 0$  fs, **c**  $\Delta t = 200$  fs and **d**  $\Delta t = 400$  fs, respectively. **e**, Momentum map of the excited states (energy integrated for  $E > E_F$  and time integrated for the first 400 fs), showing the  $K_{Gr}$  points of graphene (black box) as well as the  $K_{WSe_2}$  and  $Q_{WSe_2}$  valleys (red and green boxes, respectively). The dashed grey lines represent the hexagonal Brillouin zones of both layers. **f**, Normalized population dynamics within the

three ROIs defined in **e**:  $K_{\text{WSe}_2}$  (red) and  $Q_{\text{WSe}_2}$  (green) are populated with a  $\sim 50$  fs delay with respect to  $K_{\text{Gr}}$  (black). **g**, Schematic of the early time carrier dynamics upon below-bandgap excitation: photogenerated hot carriers within the graphene layer are transferred to the conduction bands of  $\text{WSe}_2$  via hot electron injection after the thermalization.

### **Interlayer energy transfer: from excitons in $\text{WSe}_2$ to intraband transitions in graphene**

Next, we select a pump photon energy of  $\hbar\omega_{\text{pump}}=1.55$  eV (pump pulse duration: 35 fs FWHM, pump fluence:  $F = 1.7$  mJ/cm<sup>2</sup>), near-resonant to the A-excitonic transition of  $\text{WSe}_2$ . In this case, the pump photon energy allows both the  $\text{WSe}_2$  and the graphene layer to be simultaneously photoexcited. One striking observation is that the energy distribution of excited carriers at the  $K_{\text{WSe}_2}$  valleys is centred at 0.63 eV (Fig. 3a),  $\sim 100$  meV lower than with below-bandgap excitation (Fig. 3b), as apparent from the energy distribution curves (EDCs) (first 100 fs). As discussed above, with 1.2 eV excitation, the  $K_{\text{WSe}_2}$  valleys are filled with quasi-free electrons that have tunneled from the graphene layer. Therefore, this  $\sim 100$  meV energy difference is a direct photoemission signature of exciton formation, when near-resonantly pumping using 1.55 eV photons<sup>37</sup>: the bound electron-hole (el-h) pair reduces the quasi-free particle bandgap by the exciton binding energy. In addition to this excitonic feature, we also observe a transient shift of  $\text{WSe}_2$  valence bands. In Fig. 3d, EDCs at  $K_{\text{WSe}_2}$  are shown at  $\Delta t = 0$  fs (red) and  $\Delta t = -200$  fs (black), in which the top two valence bands, VB1 and VB2, are fitted using Gaussian lineshape functions (see SI). The peak position of VB1 shifts towards the conduction band within the first 100 fs, transiently shrinking the electronic bandgap. This is due to the arrival of ICT-induced charge carriers from the

graphene layer. With near-resonantly pumping the A-exciton, the occurrence of ICT and injection of quasi-free carriers from graphene to WSe<sub>2</sub> is expected, similar to the case of below-bandgap excitation. This could lead to dynamical screening effect and the observed bandgap renormalization, as reported in highly-excited or doped ML TMDC materials<sup>38-42</sup>. As the magnitude of such a transient bandgap renormalization has been shown to scale with the excited charge carrier density<sup>40,43</sup>, we utilize the VB shift in the following as a measure of the ICT transferred carriers dynamics from graphene layer.

In addition to the excited-state dynamics in WSe<sub>2</sub>, important insight can be drawn from the energy-momentum distribution of hot carriers in graphene. As shown in the early-time 2D differential spectrum  $\Delta I(E, k, \Delta t = 0 \text{ fs})$  (Fig. 3c), obtained by subtracting the spectrum at negative time, hot carriers distribute in a broad energy range. The momentum-integrated spectrum along the linearly dispersing band in Fig. 3e clearly features the energy distribution of net electron gain (positive; red area) and loss (negative; blue area) following near-resonant photoexcitation. Remarkably, besides the modification of the distribution function near the Fermi level, we notice a strong negative peak at  $E - E_F = -1.8 \text{ eV}$ . As noted earlier, for direct photoexcitation in graphene the photoexcited carriers are expected to be spread  $\pm 0.77 \text{ eV}$  ( $\hbar\omega_{pump}/2$ ) around the Dirac point and quickly relax back to the Fermi level. Thus, this simple excitation mechanism cannot explain this peculiar feature in the valence band spectrum. The electron-electron scattering and Auger recombination could lead to a transient broadening of the momentum-space carrier distribution, but without any preferential energy localization<sup>36,44,45</sup>. Interlayer hot *hole* transfer can also be ruled out, as the top valence band of WSe<sub>2</sub> lies at  $E - E_F = -1.0 \text{ eV}$ . It would require a multi-phonon absorption

to populate the hole-states localized deeply in the valence band, taking the typical phonon energy of  $\sim 0.17$  eV in graphene<sup>46</sup>, a process of very low probability. However, the energy difference of deep-lying valence holes ( $E - E_F = -1.8$  eV) and states near  $E_F$  ( $E - E_F = -0.2$  eV) in graphene well matches the energy of the A-exciton in WSe<sub>2</sub> ( $E_{ex} \sim 1.6$  eV). Combined with the fast depletion of exciton population shown in Fig.4a (black curve) extracted from the excited state of WSe<sub>2</sub> (ROI<sub>1</sub> in Fig.3c), this brings about the following scenario for the excitation of these carriers: annihilation of excitons in WSe<sub>2</sub> drives the intraband excitation of deep-lying valence electrons in graphene into empty hole states below the Dirac point. In more detail, this exciton energy transfer process, which we term Meitner-Auger energy transfer<sup>47,48</sup>, considers recombination of excitons in WSe<sub>2</sub> with center-of-mass (COM) momentum  $\mathbf{Q}$  and exciton energy  $E_{ex}$ . The photoexcitation prepares the required hot hole vacancy below  $E_F$  in graphene, thus enabling the intraband excitation. The momentum of the valence electron-hole pair  $k_{Gr}$  is determined by the Fermi velocity of the graphene bands and the transition energy  $E_{Gr}$ . This required momentum is provided by the optically pumped excitons which gain finite COM momenta during the population formation process via phonon-mediated dephasing and intravalley thermalization<sup>49-52</sup> (see the discussion in SI). The highly efficient IET of the excitons and intraband electron-hole pairs is thus possible under the conservation of energy and momentum, *i.e.*,  $E_{ex} = E_{Gr}$  and  $\mathbf{Q} = k_{Gr}$ . In a similar trARPES study of a ML WS<sub>2</sub>/graphene heterostructure, dominating interfacial charge transfer has been observed<sup>17</sup>. Compared with our study, the different charge transfer rates could be raised from the different band structure alignment near the interface and the density of defect-sites<sup>26</sup>. While the additional exciton energy transfer was not excluded, its relative efficiency might

be reduced due to the larger COM momentum required at the larger A-exciton energy of  $\text{WS}_2$  and the energy level alignment of these specific samples.

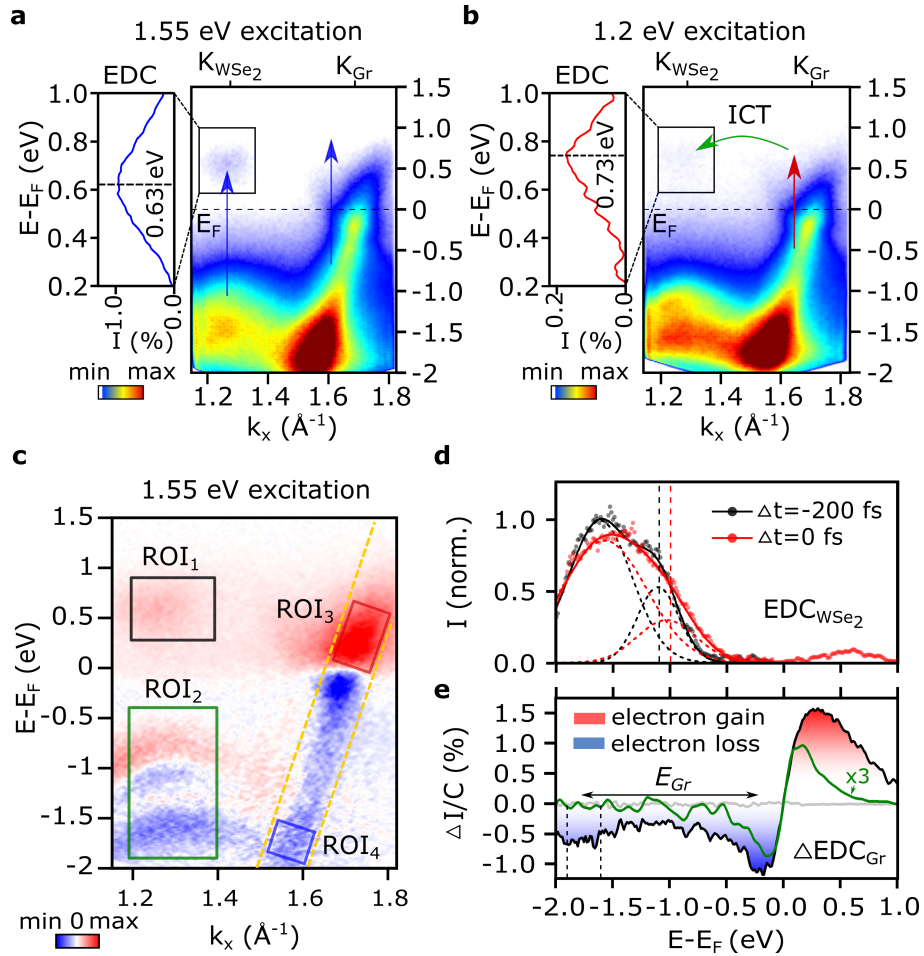


**Fig. 3: Photoemission signatures of exciton formation and interfacial interactions.** **a**, With near-resonant A-exciton pump (1.55 eV), carriers within both the  $\text{WSe}_2$  and the graphene layer are photoexcited (time integration of 100 fs). The energy of the excited-states carriers at  $K_{\text{WSe}_2}$  is 0.63 eV, shown in the EDC (left panel figure). **b**, With below-bandgap excitation (1.2 eV), the local CBM of  $K_{\text{WSe}_2}$  is filled with ICT-induced electrons and centered at 0.73 eV. **c**, Differential energy-momentum cut with 1.55 eV pump at

time zero, obtained by subtracting the negative time delay spectrum. **d**, The normalized EDC of  $K_{\text{WSe}_2}$  (momentum integration of  $0.2 \text{ \AA}^{-1}$ ) at  $\Delta t = -200 \text{ fs}$  (black) and  $\Delta t = 0 \text{ fs}$  (red). The VBs are fitted with two Gaussian functions (dashed curves) and the positions of VB1 are indicated by the dash lines. **e**, The momentum-integrated spectrum of graphene Dirac bands (between the dashed yellow lines in **c**) shows the electron gain (positive, red area) and loss (negative, blue area) following photoexcitation. The intensity is normalized by the total electron count  $C$  obtained from negative time delay spectrum. Apart from the carriers accumulation near the  $E_F$ , the hole population forms another prominent peak around  $E - E_F = -1.8 \text{ eV}$ , indicated between the dash lines. The EDC of graphene with  $1.2 \text{ eV}$  pump (green) is also shown as a comparison.

In order to gain information on the time scales of the energy and charge transfer processes, next we analyze the dynamics of excited-state populations extracted from the ROIs shown in Fig. 3c, including the excited-state carriers in  $\text{WSe}_2$  (ROI<sub>1</sub>), VB1 shifting (ROI<sub>2</sub>), hot electrons in graphene (ROI<sub>3</sub>) and IET-driven deep valence band holes (ROI<sub>4</sub>). The time trace of hot carriers in the CBM of  $\text{WSe}_2$  (black curve in Fig.4a) contains two types of quasi-particles dynamics: the photo-generated excitons  $N_T^{ex}$  and the ICT-induced quasi-free electrons  $N_T^{el}$ . The decay of excitons excite the valence band electrons in graphene via IET with a transfer time of  $\tau_{IET}$  (Fig. 4f). On the other hand, the arrival of ICT-induced electrons transiently shifts the VBs of  $\text{WSe}_2$  (green curve in Fig.4a) which therefore represents the dynamics of  $N_T^{el}$  as discussed before. We assume VB1 and VB2 shift in the same way (fitting details see SI). The VB1 shifting shows a time delay of  $\sim 65 \text{ fs}$  compared to the CB signal, evidencing the occurrence of interlayer hot electron injection after pho-

to excitation. The population of  $N_T^{el}$  subsequently relaxes back to  $K_{Gr}$ , refilling the excited-states of graphene (Fig. 4h). From the graphene side, the photoexcited hot electrons  $N_{Gr}^{el}$  (red curve in Fig. 4b) could either scatter to conduction bands of WSe<sub>2</sub> or relax by interband decay channels in graphene. Therefore, the relaxation of  $N_{Gr}^{el}$  could be characterized with the charge transfer time of  $\tau_{ICT}$  and a decay time of  $\tau_{Gr}^{el}$ . The deep valence band holes  $N_{Gr}^h$  (blue curve in Fig. 4b) are populated by exciton energy transfer on a time scale of  $\tau_{IET}$ , which would relax back to the Fermi level with a lifetime of  $\tau_{Gr}^h$ .

The complete dynamics across the interface can be described with a set of coupled rate equations based on a multi-level scheme (details see SI). By numerically solving the rate equation model, we disentangle the dynamics of IET and ICT. Our global fit describes the data well and yields the transfer times of  $\tau_{IET} = 67 \pm 7$  fs and  $\tau_{ICT} = 118 \pm 18$  fs. The lifetimes of electrons and IET-populated hot holes in graphene are simultaneously extracted as  $\tau_{Gr}^{el} = 84 \pm 7$  fs and  $\tau_{Gr}^h = 7 \pm 4$  fs. Combining all our observations and analysis of the energy-momentum dynamics in WSe<sub>2</sub> and graphene, we summarize the interfacial phenomena governing the non-equilibrium behaviour of our heterostructure: first, the optical pump generates excitons in WSe<sub>2</sub> and quasi-free carriers in graphene (Fig. 4e). Following photoexcitation, the exciton annihilation excites deep valence electrons in graphene via an IET process (Fig. 4f-g). Simultaneously, hot electrons in graphene are injected to the conduction bands of WSe<sub>2</sub> via ICT which transiently shift the valence bands of WSe<sub>2</sub> (Fig. 4h).

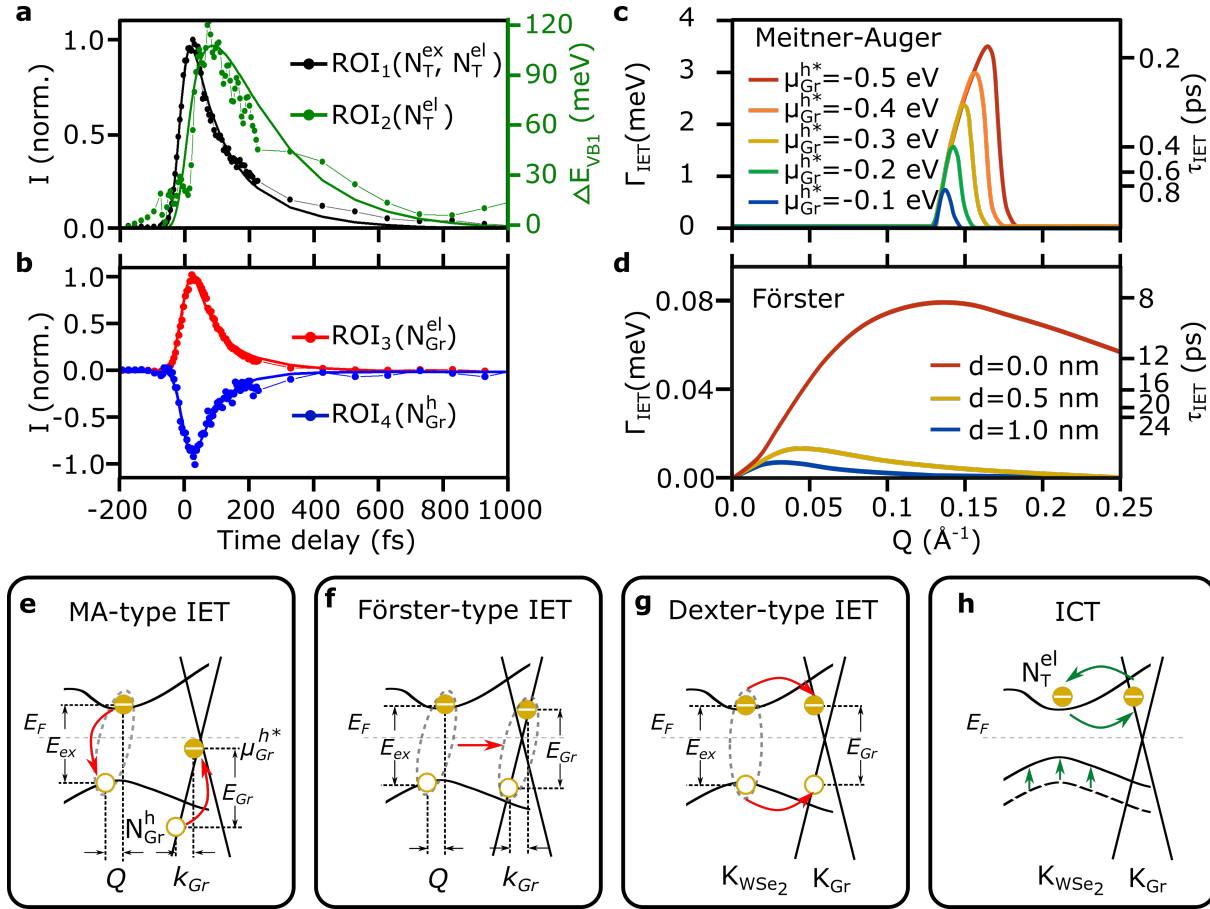


**Fig. 4: Interlayer charge and energy transfer upon near-resonant A-exciton excitation.** **a**, By integrating the ROI<sub>1</sub> in Fig.3c, the time trace of the normalized photoemission intensity of excited-state carriers at the CBM of WSe<sub>2</sub> (black) contains the dynamics of excitons ( $N_T^{ex}$ ) and ICT-induced quasi-free carriers ( $N_T^{el}$ ). The energy shift of VB1 (green) mainly reflects the dynamic of  $N_T^{el}$ , which are extracted from time-dependent EDCs in ROI<sub>2</sub>. **b**, The time traces of hot electrons (red) and hot holes in the deep VB (blue) in graphene are extracted from the ROI<sub>3</sub> and ROI<sub>4</sub> in Fig.3c, respectively. The time traces in **a-b** are fitted globally based on a rate equation model (see text). **c**, Calculated Meitner-Auger mediated IET transfer rate as a function of COM momentum  $Q$  with different photo-



induced hole vacancy at  $E = \mu_{Gr}^{h*}$ . **d**, Calculated Förster coupling rate as a function of  $Q$  with varied interlayer distance of  $d$ . Sketch of the underlying carrier dynamics: **e**, Meitner-Auger IET with creation of intraband electron-hole pairs in graphene by absorbing the exciton energy. **f**, Förster-type energy transfer with generation of interband electron-hole pairs in graphene. **g**, Dexter-type energy transfer with electrons and holes injection to graphene simultaneously. **h**, ICT-induced hot electron injection into  $WSe_2$  and transient energy shift of its valence band.

To elucidate the interfacial coupling mechanism at play in our experiment, in particular the observed ultrafast energy transfer rate, we perform microscopic calculations of three types of IET mechanisms: Meitner-Auger, Förster and Dexter energy transfer. The interlayer MA process is described by the dipole-monopole energy transfer from excitons to valence band excitation, schematically shown in Fig. 4e. The photoexcited hot holes in graphene quickly relax and distribute below  $E_F$  near a transient chemical potential  $\mu_{Gr}^{h*}$ . This allows an MA-type transition from the deep valence band to the hot hole vacancy by absorbing the exciton energy. The microscopically calculated transfer rate is plotted as a function of  $Q$  in Fig.4c with different transient chemical potentials for the hole distributions  $\mu_{Gr}^{h*}$ . When the hole vacancy is located around  $\mu_{Gr}^{h*} = -0.3$  eV, the maximum transfer rate reaches  $\Gamma_{IET} = 2.4$  meV, corresponding to a  $\tau_{IET} = 270$  fs transfer time. The MA-type IET process could describe the observed energy-momentum distribution of intraband transition of valence electrons in a reasonable quantitative agreement with the extracted transfer rate.

Another IET mechanism is Förster energy transfer (Fig.4f). The energy of the exciton excites

an *interband* transition from valence bands to above Dirac point via the dipole-dipole coupling.<sup>53</sup> In contrast to the MA-type IET process, the interband excitation via Förster-type energy transfer populates the conduction bands of graphene above the Fermi level, independent of the photon-induced hot carriers distribution. The coupling strength is explicitly evaluated (for derivation, see SI) and determined by the momentum  $\mathbf{Q}$  and interlayer distance  $d$ . The strong exciton oscillator strength and intrinsic in-plane exciton dipole moment in many 2D materials favor the Förster-type IET<sup>54</sup>. However, the calculated transfer rate is only 0.08 meV (a transfer time of  $\sim 8.1$  ps), even assuming a tightly stacked heterostructure with interlayer distance of  $d = 0$  nm (Fig.4d). Our calculations reveal that the IET process preferably excites an *intraband* rather than an *interband* transition. The experimentally observed energy-momentum distribution of excited-state hot holes supports this conclusion. In addition, we also performed calculations of Dexter-type IET (Fig.4g), in which scenario the electron and hole components of excitons in WSe<sub>2</sub> scatter to the graphene layer simultaneously. However, due to the small wavefunction overlap and the finite momentum distance between  $K_{\text{WSe}_2}$  and  $K_{\text{Gr}}$ , we found a very weak Dexter-type interlayer coupling strength, more than three orders of magnitude smaller compared to the other two mechanisms (see SI). We can thus identify the MA-type conversion of excitons in WSe<sub>2</sub> to intraband excitations in graphene as the dominant IET mechanism.

In this work, we provide a detailed microscopic picture of interfacial charge and energy transfer processes in photoexcited ML-WSe<sub>2</sub>/graphene heterostructures. Optical excitation of electrons in graphene leads to inter-layer charge transfer of quasi-free electrons from the graphene layer to the K and Q valleys of the semiconductor's conduction bands on a time scale of  $\sim 50$  fs. In con-

trast, excitons in WSe<sub>2</sub> decay through an interfacial Meitner-Auger energy transfer process with a time constant of  $\sim 70$  fs. This previously unidentified process is governed by inter-layer dipole-monopole interactions leading to annihilation of an exciton in WSe<sub>2</sub> and *non-vertical intraband* excitations in graphene. The momentum of the electron-hole pair in graphene originates from the finite center of mass momentum of the hot excitons in WSe<sub>2</sub>. The interfacial Meitner-Auger mechanism is found to dominate the energy transfer process over established mechanisms like Förster- and Dexter-type transfer. This mechanism results in transient hole distributions as low as 2 eV below the Dirac points. These observations enrich the physical toolbox for designing van der Waals heterostructures and might be utilized in hot-carrier photovoltaic device concepts to harness the ultrafast and efficient carrier transfer processes at interfaces<sup>55</sup>.

## Methods

**Time- and angle-resolved photoemission spectroscopy** We used a 500kHz tabletop femtosecond optical parametric chirped pulse amplification (OPCPA) laser system operated at a center wavelength of 800 nm and delivering average power up to 15 W. The high harmonic generation is produced in a vacuum chamber by tight focusing (10  $\mu\text{m}$ ) the second harmonic (400 nm) of the OPCPA fundamental on a thin and dense argon gas jet. We select the photons around 21.7 eV (110 meV FWHM bandwidth) as the probe arm for trARPES experiment<sup>27</sup>. Concerning the pump arm, we used two different beams for this study. One pump beam is directly obtained from the OPCPA (800 nm, FWHM=35 fs) and another one is the residual power of the compressed fiber amplifier (1030 nm, FWHM=200 fs). The pump and probe beams are coupled into an ultra-high-

vacuum (UHV) chamber and spatially overlapped at the sample position which is controlled by a six-axis manipulator (Carving, SPECS GmbH). The main UHV chamber is equipped with an unique combination of a hemispherical electron energy analyzer (PHOIBOS150, SPECS GmbH) and time-of-flight (ToF) momentum microscope (METIS1000, SPECS GmbH)<sup>28</sup>. On the one hand, the hemispherical analyzer, which can work in a multi-electrons per laser shot regime, provides high statistic energy/momentum cuts along a given momentum direction, as shown in Fig.3. On the other hand, the momentum microscope allows for efficient, parallel, momentum-resolved detection of the full photoemission horizon from the surface as shown in Fig.1b and Fig.2a-e. All the experiments are performed at room temperature.

**ML-WSe<sub>2</sub>/ML-Graphene vdW heterostructure fabrication** Monolayer graphene on SiC (Si-terminated surface) was grown using the well-established recipe of sublimation growth at elevated temperatures in an argon atmosphere<sup>4</sup>. Note that, on SiC<sup>56</sup>, the graphene monolayer resides on top of a  $(6\sqrt{3} \times 6\sqrt{3})R30^\circ$  reconstructed carbon buffer layer that is covalently bound to the SiC substrate. WSe<sub>2</sub> films were grown on the thus prepared MLG/SiC substrates via hybrid-pulsed-laser deposition (hPLD) in ultra-high vacuum<sup>33</sup>. Pure tungsten (99.99%) was ablated using a pulsed KrF excimer laser (248 nm) with a repetition rate of 10 Hz, while pure selenium (99.999%) was evaporated from a Knudsen cell at a flux rate of around 1.5 Å/s as monitored by a quartz crystal microbalance. The deposition was carried out at 450°C for 6 h, followed by two-step annealing at 640°C and 400°C for 1 h each.

**DFT calculation of band structure** We performed density functional theory (DFT) calculation of suspended ML WSe<sub>2</sub> and graphene with the projector augmented wave code GPAW<sup>57</sup> using

GLLB-SC xc-functional, separately. The GLLB-SC is an orbital-dependent exact exchange-based functional including the spin-orbital coupling<sup>58</sup>. The relaxed lattice constant of WSe<sub>2</sub> is  $a=3.25 \text{ \AA}$ . We sample the Brillouin Zone with a  $(15 \times 15 \times 1)$  k-point mesh, and set the cutoff energy for the plane-wave expansion at 600 eV. The bandgap is adjusted to fit our data. The calculated band structures of both materials are superimposed on each other and shown in Fig.2a.

### **Data availability**

All data underlying this study are available from the Zenodo repository. Source data are provided with this paper.

## References

1. Novoselov, K.S., Mishchenko, A., Carvalho, A. & Neto, A. H. 2D materials and van der Waals heterostructures. *Science* **353**, 6298 (2016).
2. Akinwande, D. *et al.* Graphene and two-dimensional materials for silicon technology. *Nature* **573**, 507–518 (2019).
3. Liu, F. *et al.* Disassembling 2D van der Waals crystals into macroscopic monolayers and reassembling into artificial lattices. *Science* **367**, 903–906 (2020).
4. Emtsev, K. V. *et al.* Towards wafer-size graphene layers by atmospheric pressure graphitization of silicon carbide. *Nat. Mater.* **8**, 203–207 (2009).
5. Jin, C. *et al.* Ultrafast dynamics in van der Waals heterostructures. *Nat. Nanotechnol.* **13**, 994–1003 (2018).
6. Lee, C.-H. *et al.* Atomically thin p–n junctions with van der Waals heterointerfaces. *Nat. Nanotechnol.* **9**, 676 (2014).
7. McGilly, L. J. *et al.* Visualization of moiré superlattices. *Nat. Nanotechnol.* **15**, 580–584 (2020).
8. Cao, Y. *et al.* Unconventional superconductivity in magic-angle graphene superlattices. *Nature* **556**, 43–50 (2018).
9. Kunstmann, J. *et al.* Momentum-space indirect interlayer excitons in transition-metal dichalcogenide van der Waals heterostructures. *Nat. Phys.* **14**, 801–805 (2018).

10. Rivera, P. *et al.* Observation of long-lived interlayer excitons in monolayer MoSe<sub>2</sub>–WSe<sub>2</sub> heterostructures. *Nat. Commun.* **6**, 6242 (2015).
11. Binder, J. *et al.* Upconverted electroluminescence via auger scattering of interlayer excitons in van der Waals heterostructures. *Nat. Commun.* **10**, 2335 (2019).
12. Avsar, A. *et al.* Spin–orbit proximity effect in graphene. *Nat. Commun.* **5**, 4875 (2014).
13. Garcia, J. H., Vila, M., Cummings, A. W. & Roche, S. Spin transport in graphene/transition metal dichalcogenide heterostructures. *Chem. Soc. Rev.* **47**, 3359–3379 (2018).
14. Massicotte, M. *et al.* Photo-thermionic effect in vertical graphene heterostructures. *Nat. Commun.* **7**, 12174 (2016).
15. Selig, M., Malic, E., Ahn, K. J., Koch, N. & Knorr, A. Theory of optically induced Förster coupling in van der Waals coupled heterostructures. *Phys. Rev. B* **99**, 035420 (2019).
16. Froehlicher, G., Lorchat, E. & Berciaud, S. Charge versus energy transfer in atomically thin graphene-transition metal dichalcogenide van der Waals heterostructures. *Phys. Rev. X* **8**, 011007 (2018).
17. Aeschlimann, S. *et al.* Direct evidence for efficient ultrafast charge separation in epitaxial WS<sub>2</sub>/graphene heterostructures. *Sci. Adv.* **6**, 0761 (2020).
18. Hill, H. M. *et al.* Exciton broadening in WS<sub>2</sub>/graphene heterostructures. *Phys. Rev. B* **96**, 205401 (2017).

19. Ferrante, C. *et al.* Picosecond energy transfer in a transition metal dichalcogenide-graphene heterostructure revealed by transient Raman spectroscopy. *PNAS* **119**, 15 (2022).
20. Luo, D. *et al.* Twist-angle-dependent ultrafast charge transfer in MoS<sub>2</sub>-graphene van der Waals heterostructures. *Nano Lett.* **21**, 8051–8057 (2021).
21. He, J. *et al.* Electron transfer and coupling in graphene–tungsten disulfide van der Waals heterostructures. *Nat. Commun.* **5**, 5622 (2014).
22. Krause, R. *et al.* Ultrafast charge separation in bilayer WS<sub>2</sub>/graphene heterostructure revealed by time-and angle-resolved photoemission spectroscopy. *Front. Phys.* **2021**, 668149 (2021).
23. Zhou, H., Chen, Y. & Zhu, H. Deciphering asymmetric charge transfer at transition metal dichalcogenide–graphene interface by helicity-resolved ultrafast spectroscopy. *Sci. Adv.* **7**, 34 (2021).
24. Yuan, L. *et al.* Photocarrier generation from interlayer charge-transfer transitions in WS<sub>2</sub>-graphene heterostructures. *Sci. Adv.* **4**, 1700324 (2018).
25. Fu, S. *et al.* Long-lived charge separation following pump-wavelength–dependent ultrafast charge transfer in graphene/WS<sub>2</sub> heterostructures. *Sci. Adv.* **7**, 9 (2021).
26. Krause, R. *et al.* Microscopic understanding of ultrafast charge transfer in van-der-Waals heterostructures. *Phys. Rev. Lett.* **127**, 276401 (2021).
27. Puppin, M. *et al.* Time-and angle-resolved photoemission spectroscopy of solids in the extreme ultraviolet at 500 kHz repetition rate. *Rev. Sci. Instrum.* **90**, 023104 (2019).



28. Maklar, J. *et al.* A quantitative comparison of time-of-flight momentum microscopes and hemispherical analyzers for time-resolved ARPES experiments *Rev. Sci. Instrum.* **91**, 123112 (2020).
29. Li, Y. *et al.* Measurement of the optical dielectric function of monolayer transition-metal dichalcogenides: MoS<sub>2</sub>, MoSe<sub>2</sub>, WS<sub>2</sub>, and WSe<sub>2</sub>. *Phys. Rev. B* **90**, 205422 (2014).
30. Wallauer, R. *et al.* Momentum-resolved observation of exciton formation dynamics in monolayer WS<sub>2</sub>. *Nano Lett.* **21**, 5867–5873 (2021).
31. Madéo, J. *et al.* Directly visualizing the momentum-forbidden dark excitons and their dynamics in atomically thin semiconductors. *Science* **370**, 1199–1204 (2020).
32. Bostwick, A., Ohta, T., Seyller, T., Horn, K. & Rotenberg, E. Quasiparticle dynamics in graphene. *Nat. Phys.* **3**, 36–40 (2007).
33. Nakamura, H. *et al.* Spin splitting and strain in epitaxial monolayer WSe<sub>2</sub> on graphene. *Phys. Rev. B* **101**, 165103 (2020).
34. Baudisch, M. *et al.* Ultrafast nonlinear optical response of Dirac fermions in graphene. *Nat. Commun.* **9**, 1018 (2018).
35. Breusing, M., Ropers, C. & Elsaesser, T. Ultrafast carrier dynamics in graphite. *Phys. Rev. Lett.* **102**, 086809 (2009).
36. Chen, Y., Li, Y., Zhao, Y., Zhou, H. & Zhu, H. Highly efficient hot electron harvesting from graphene before electron-hole thermalization. *Sci. Adv.* **5**, 9958 (2019).

37. Dong, S. *et al.* Direct measurement of key exciton properties: Energy, dynamics, and spatial distribution of the wave function. *Nat. Sci.* **1**,e10010 (2021).
38. Chernikov, A., Ruppert, C., Hill, H. M., Rigosi, A. F. & Heinz, T. F. Population inversion and giant bandgap renormalization in atomically thin WS<sub>2</sub> layers. *Nat. Photonics* **9**, 466–470 (2015).
39. Liu, F., Ziffer, M. E., Hansen, K. R., Wang, J. & Zhu, X. Direct determination of band-gap renormalization in the photoexcited monolayer MoS<sub>2</sub>. *Phys. Rev. Lett.* **122**, 246803 (2019).
40. Gao, S., Liang, Y., Spataru, C. D. & Yang, L. Dynamical excitonic effects in doped two-dimensional semiconductors. *Nano Lett.* **16**, 5568–5573 (2016).
41. Dendzik, M. *et al.* Observation of an excitonic Mott transition through ultrafast core-*cum*-conduction photoemission spectroscopy. *Phys. Rev. Lett.* **125**, 096401 (2020).
42. Steinhoff, A., Rosner, M., Jahnke, F., Wehling, T. O. & Gies, C. Influence of excited carriers on the optical and electronic properties of MoS<sub>2</sub>. *Nano Lett.* **14**, 3743–3748 (2014).
43. Liang, Y. & Yang, L. Carrier plasmon induced nonlinear band gap renormalization in two-dimensional semiconductors. *Phys. Rev. Lett.* **114**, 063001 (2015).
44. Tomadin, A., Brida, D., Cerullo, G., Ferrari, A. C. & Polini, M. Nonequilibrium dynamics of photoexcited electrons in graphene: Collinear scattering, Auger processes, and the impact of screening. *Phys. Rev. B* **88**, 035430 (2013).

45. Gierz, I., Link, S., Starke, U. & Cavalleri, A. Non-equilibrium Dirac carrier dynamics in graphene investigated with time- and angle-resolved photoemission spectroscopy. *Faraday Discuss.* **171**, 311–321 (2014).
46. Na, M. *et al.* Direct determination of mode-projected electron-phonon coupling in the time domain. *Science* **366**, 1231–1236 (2019).
47. Meitner, L. On the origin of the  $\beta$ -ray spectra of radioactive substances. *Z. Phys.* **9**, 131–144 (1922).
48. Auger, P. Sur les rayons  $\beta$  secondaires produits dans un gaz par des rayons X. *CR Acad. Sci.(F)* **177**, 169 (1923).
49. Selig, M. *et al.* Excitonic linewidth and coherence lifetime in monolayer transition metal dichalcogenides. *Nat. Commun.* **7**, 13279 (2016).
50. Christiansen, D., Selig, M., Malic, E., Ernstorfer, R. & Knorr, A. Theory of exciton dynamics in time-resolved ARPES: Intra- and intervalley scattering in two-dimensional semiconductors. *Phys. Rev. B* **100**, 205401 (2019).
51. Selig, M. *et al.* Ultrafast dynamics in monolayer transition metal dichalcogenides: Interplay of dark excitons, phonons, and intervalley exchange. *Phys. Rev. Res.* **1**, 022007 (2019).
52. Pöllmann, C. *et al.* Resonant internal quantum transitions and femtosecond radiative decay of excitons in monolayer WSe<sub>2</sub>. *Nat. Mater.* **14**, 889–893 (2015).
53. Förster, T. Intermolecular energy migration and fluorescence. *Ann. Phys.* **437**, 55–75 (1948).

54. Kozawa, D. *et al.* Evidence for fast interlayer energy transfer in MoSe<sub>2</sub>/WS<sub>2</sub> heterostructures. *Nano Lett.* **16**, 4087–4093 (2016).
55. Paul, K. K., Kim, J.-H. & Lee, Y. H. Hot carrier photovoltaics in van der Waals heterostructures. *Nat. Rev. Phys.* **3**, 178–192 (2021).
56. Riedl, C., Coletti, C. & Starke, U. Structural and electronic properties of epitaxial graphene on SiC (0 0 0 1): a review of growth, characterization, transfer doping and hydrogen intercalation. *J. Phys. D: Appl. Phys.* **43**, 374009 (2010).
57. Mortensen, J. J., Hansen, L. B. & Jacobsen, K. W. Real-space grid implementation of the projector augmented wave method. *Phys. Rev. B* **71**, 035109 (2005).
58. Gritsenko, O., van Leeuwen, R., van Lenthe, E. & Baerends, E. J. Self-consistent approximation to the kohn-sham exchange potential. *Phys. Rev. A* **51**, 1944 (1995).

**Acknowledgements** This work was funded by the Max Planck Society, the European Research Council (ERC) under the European Union’s Horizon 2020 research and innovation program (Grant No. ERC-2015-CoG-682843), the German Research Foundation (DFG) within the Emmy Noether program (Grant No. RE 3977/1), through Projektnummer 18208777-SFB 951 ”Hybrid Inorganic/Organic Systems for Opto-Electronics (HIOS)” (CRC 951 project B12, M.S., D.C., A.K.), and the SFB/TRR 227 ”Ultrafast 264 Spin Dynamics” (projects A09 and B07). S.B. acknowledges financial support from the NSERC-Banting Postdoctoral Fellowships Program. M.D. acknowledges financial support from the Göran Gustafssons Foundation. K.W. and T.T. acknowledge support from the Elemental Strategy Initiative conducted by the MEXT, Japan (Grant Number JPMXP0112101001) and JSPS KAKENHI (Grant Numbers 19H05790

and JP20H00354).

**Author contributions** S.D., S.B., T.P., M.D., J.M., A.N. and L.R. performed the trARPES measurement. S.D. analyzed the data and wrote the first draft of the manuscript. R.E., L.R. and M.W. were responsible for developing all the experimental infrastructures. M.S. and D.C. performed the microscopic calculation with the guidance of A.K.. R.P.X. developed the 4D data processing code. P.R. and H.N. provided the epitaxially-grown heterostructure, with support from U.S. and H.T.. A.M., A.S., and M.S. conducted Raman and photoluminescence measurements, with guidance from M.J and P.M.. J.D.Z and A.C. prepared the exfoliated ML sample with the hBN substrate provided by K.W. and T.T.. All authors contributed to the final version of the manuscript.

**Competing Interests** The authors declare that they have no competing financial interests.

**Correspondence** Correspondence and requests for materials should be addressed to [dong@fhi-berlin.mpg.de](mailto:dong@fhi-berlin.mpg.de), [rettig@fhi-berlin.mpg.de](mailto:rettig@fhi-berlin.mpg.de) and [ernstorfer@fhi-berlin.mpg.de](mailto:ernstorfer@fhi-berlin.mpg.de).